Fine structure study of $A\beta_{1-42}$ fibrillogenesis with atomic force microscopy

Muriel Arimon,* Ismael Díez-Pérez,[†] Marcelo J. Kogan,[‡,1] Núria Durany,[§] Ernest Giralt,[‡,‖] Fausto Sanz,[†] and Xavier Fernàndez-Busquets*

*Laboratori de Recerca en Nanobioenginyeria, Parc Científic de Barcelona, Universitat de Barcelona; [†]Departament de Química Física, Universitat de Barcelona; [‡]Institut de Recerca Biomèdica de Barcelona, Parc Científic de Barcelona; [§]Facultat de Ciències de la Salut, Universitat Internacional de Catalunya, Barcelona; and [‖]Departament de Química Orgànica, Universitat de Barcelona, Barcelona, Spain

[1]Present address: Departamento de Química Farmacológica y Toxicológica, Facultad de Ciencias Químicas y Farmacéuticas, Universidad de Chile, Santiago, Chile

Corresponding author: X. Fernàndez-Busquets, Research Center for Bioelectronics and Nanobioscience, Barcelona Science Park, Josep Samitier 1-5, E-08028 Barcelona, Spain. E-mail: xfernandez_busquets@ub.edu

ABSTRACT

One of the hallmarks of Alzheimer's disease is the self-aggregation of the amyloid β peptide (Aβ) in extracellular amyloid fibrils. Among the different forms of Aβ, the 42-residue fragment ($A\beta_{1-42}$) readily self-associates and forms nucleation centers from where fibrils can quickly grow. The strong tendency of $A\beta_{1–42}$ to aggregate is one of the reasons for the scarcity of data on its fibril formation process. We have used atomic force microscopy (AFM) to visualize in liquid environment the fibrillogenesis of synthetic $A\beta_{1–42}$ on hydrophilic and hydrophobic surfaces. The results presented provide nanometric resolution of the main structures characteristic of the several steps from monomeric $A\beta_{1–42}$ to mature fibrils in vitro. Oligomeric globular aggregates of $A\beta_{1–42}$ precede the appearance of protofibrils, the first fibrillar species, although we have not obtained direct evidence of oligomer-protofibril interconversion. The protofibril dimensions deduced from our AFM images are consistent with a model that postulates the stacking of the peptide in a hairpin conformation perpendicular to the long axis of the protofibril, forming single β-sheets ribbon-shaped. The most abundant form of $A\beta_{1–42}$ fibril exhibits a nodular structure with a ~100-nm periodicity. This length is very similar *1)* to the length of protofibril bundles that are the dominant feature at earlier stages in the aggregation process, *2)* to the period of helical structures that have been observed in the core of fibrils, and *3)* to the distance between regularly spaced, structurally weak fibril points. Taken together, these data are consistent with the existence of a ~100-nm long basic protofibril unit that is a key fibril building block.

Key words: amyloid-beta peptide • Alzheimer • amyloid-beta fibrils • amyloid-beta protofibrils

Pathogenesis in Alzheimer's disease (AD) is linked to the accumulation of the highly amyloidogenic self-associating amyloid β_{1-42} peptide ($A\beta_{1-42}$). $A\beta_{1-42}$ is one of a family of peptides derived from the amyloid precursor protein (APP) through the action of a series of membrane-bound proteases. The function of APP itself is unknown, nor is the Aβ-induced neurodegenerative pathway. Some of the potentially cytotoxic processes in which a role for Aβ has been postulated include the promotion of oxidative stress (1), the formation of Ca^{2+}-permeable channels in the cell membrane (2–4), the targeting and functional disruption of particular synapses by Aβ oligomers (5), and the triggering of synthesis and release of toxic molecules such as nitric oxide (6). Current data have shown that soluble Aβ oligomers ranging from trimers to 24mers, termed ADDLs (amyloid derived diffusible ligands), may be the key effectors of cytotoxicity in AD (5, 7–10). In neuroblastoma cell viability assays, ADDLs inhibited neuronal viability 10-fold more than fibrils and ~40-fold more than unaggregated peptides (10). Other evidence, however, indicates that the neurotoxic activity of Aβ requires its aggregation in fibrillar form (11, 12), although it has also been suggested that the aggregates may be a mechanism of defense acting by concealing and immobilizing neurotoxic soluble Aβ (13). In either case, a detailed knowledge of the structure and assembly dynamics of Aβ is important for the development of properly targeted AD therapeutics. Synthetic Aβ spontaneously assembles into amyloid fibers indistinguishable from those found in the brains of Alzheimer's disease patients (see Ref. 14, and references therein), indicating that in vitro studies are a useful tool for the study of the fibrillogenesis process.

Of the several peptidic fragments derived from APP proteolysis, $A\beta_{1-42}$ is one of the most hydrophobic and neurotoxic forms of human Aβ (10, 15). Consistent with their putative role in pathogenesis, ADDLs form mainly from $A\beta_{1-42}$ (7, 9). The fibrillogenesis of a more soluble species, $A\beta_{1-40}$, has been extensively investigated (11, 12, 16–18), but the information gathered from these studies is complex because of the many different solvents and conditions used. As a result, there is no consensus, neither for the fibrillogenetic pathway from $A\beta_{1-40}$ monomers through early aggregates and on to protofibrils and fibrils, nor for the detailed structure of the intermediate and final species. On the other hand, the studies with $A\beta_{1-42}$ have been often hampered by the extreme tendency of the peptide to aggregate, and its fibril formation process remains controversial. Although it was first suggested that $A\beta_{1-40}$ and $A\beta_{1-42}$ fibrillogenesis followed identical steps (16, 19), more recent data coming from cross-linking experiments have revealed that the oligomerization of both peptides proceeds through distinct pathways (20). $A\beta_{1-42}$ fibril formation has been described in some works as a nucleation-dependent, linear sequence of events starting from monomeric peptide that coalesces to form small ADDLs that, in turn, self-assemble to form rodlike protofibrils 3-4 nm across (20). This hypothesis, however, is being challenged by data indicating that ADDL solutions are sufficiently stable to be a dead end not leading to fibrillogenesis (9). At the moment, the extent to which ADDLs exist in dynamic equilibrium with protofibrils remains unknown. Other views sustain that the β-sheet conformation of the peptide lies at the basis of protofibril formation by promoting the stacking of Aβ molecules perpendicular to the protofibril axis (11). Protofibril association and/or direct monomer or oligomer addition gives finally rise to full-length fibrils 7–8 nm in diameter (16, 18, 19). Aβ fibrils have been observed to be very polymorphic, ranging from coiled forms with a wide variety of helix periodicities to species without an evident twist (11, 16–18), but data about their fine structure are scarce.

In this work, we have used atomic force microscopy (AFM) to study in detail the in vitro genesis and structure of $A\beta_{1–42}$ fibrils. AFM permits the visualization of biological macromolecules at the nanometer scale and in liquid medium, thus allowing the inference of structural characteristics that are closer to the in vivo situation and has revealed itself as a potent tool for the study of synthetic $A\beta_{1–42}$ aggregation (3, 6–8, 14, 16, 21–25). We have taken advantage of these AFM capabilities to gain a deeper insight into the structure of the intermediate species in the process of $A\beta_{1–42}$ fibril generation in vitro.

MATERIALS AND METHODS

Preparation of $A\beta_{1–42}$

$A\beta_{1–42}$ synthesized by Peptide Institute, Inc. (Osaka, Japan) was purchased lyophilized in glass vials and stored at –80°C immediately upon arrival. For accurate concentration determination, the peptide was dissolved in deionized water (milliQ system, Millipore), sonicated at 28°C for 1 min, and amino acid analysis was performed on an automatic analyzer (Beckman System 6300, Fullerton, CA), which used ninhydrin as derivatization agent. Peptide aliquots were lyophilized again in glass vials and stored at –20°C until used. Next, to obtain a homogeneous solution free of aggregates, a variant of Zagorski's protocol (26) was followed. Briefly, $A\beta_{1–42}$ was first dissolved with trifluoroacetic acid (TFA) in the same vial where it was lyophilized, and TFA was then evaporated under a stream of N_2. To thoroughly remove TFA, 1,1,1,3,3,3-hexafluoro-2-propanol was added and evaporated 3 times, and the sample was finally left overnight in a desiccator. The dry aliquot was carefully and completely resuspended in a solution containing 10 mM phosphate buffer, pH 7.4 (PB) and 10 mM NaOH to reach a final pH of 7.4 and an $A\beta_{1–42}$ concentration of 40 μM. Before use, all solutions were filtered through a 0.20 μm pore size filter (Iwaki). Several aliquots were made and stored at –20°C until used. For each experiment, an aliquot was thawed and diluted to a concentration of 10 μM in 10 mM PB, or in 10 mM acetate buffer, pH 5.0. Samples were incubated in 1-mL Eppendorf tubes in an oven at 37°C with gentle rocking.

Electrophoresis and immunoblots

Polyacrylamide gel electrophoresis was performed as originally described by Laemmli (27), following the modified protocol of Schagger and von Jagow (28), in tricine gels containing 0.1% SDS. Immunoblots were transferred to a polyvinylidene difluoride membrane (Immobilon, Millipore) with a Mini Trans-Blot Cell (Bio-Rad), blocked in 0.1 M Tris-HCl, pH 7.5, 0.5% Tween 20, 1% Triton X-100, 3% bovine serum albumin (Sigma), and incubated in the presence of rabbit anti-$A\beta_{1-40}$ (Sigma) diluted 1:2000 in blocking solution. The enhanced chemiluminescence Western blotting detection system (Amersham, Piscataway, NJ) was used to visualize the decorated bands.

Atomic force microscopy

Imaging was performed with a commercial MultiMode atomic force microscope controlled by a Nanoscope IV electronics (Digital Instruments, Santa Barbara, CA), equipped with either a 12-μm scanner (E-scanner) or a 120-μm scanner (J-scanner). Except where otherwise indicated, all images were taken in liquid using a tapping-mode liquid cell without the O-ring seal. Oxide-

sharpened pyramidal Si_3N_4 tips mounted on triangular 100-μm long cantilevers (k=0.08 N/m) were purchased from Olympus (Tokyo, Japan). The liquid cell and the tip were cleaned with ethanol and thoroughly rinsed with deionized water before use. For high-resolution imaging, the microscope head was placed on a vibration-isolated stone plate. After the indicated incubation times and immediately before imaging, 10 μL of the sample were allowed to adsorb for ~5–10 min at room temperature on freshly cleaved muscovita mica (Asheville-Schoonmaker Mica Co., Newport News, VA) or highly ordered pyrolytic graphite (Nt-MDT Co., Zelenograd, Moscow, Russia), and finally overlaid with ~100 μL of incubation buffer. To confine this liquid volume when mica was used, an ~1 cm^2 piece of mica was glued to a Teflon support that had been previously cleaned in *piranha* solution (H_2SO_4/H_2O_2, 1:3 vol/vol) and thoroughly rinsed with distilled water. For images taken in air, the surface was carefully rinsed with deionized water and gently dried under a N_2 stream. AFM measurements of small isolated molecules are influenced by a distortion resulting from the fact that the image acquired is a convolution of the actual surface topography and the shape of the tip, resulting in an overestimation of width dimensions (29). Convolution will be significant for structures of smaller diameter than the radius of the AFM tip apex, which in our case is around 10 nm. Although complex algorithms are needed to precisely deconvolute AFM images (30), we can obtain a good estimation of the real size of the structure being scanned from a simple geometrical deconvolution model (31, 32), by treating the particle as spherical or cylindrical:

$$w = 2 \cdot (2 \cdot R_t \cdot h)^{1/2} \quad [1]$$

where w is the width or diameter observed in the AFM image, R_t is the tip apex radius, and h the real width of the structure. For the estimation of the dimensions of internal fibril structures that cannot be deconvoluted with Eq. [1], we have used the Microscope Simulator 1.0.2 software (Center for Computer Integrated Systems for Microscopy and Manipulation, CISMM, University of North Carolina). Z scale for all amplitude images is 0.2 V. Statistical analysis was done with the Origin 6.0 software package.

Transmission electron microscopy

Samples were adsorbed on Formvar/carbon-coated grids and negatively stained with 2% uranyl acetate. They were observed in a Jeol 1010 transmission electron microscope, and images were digitized with a SIS Megaview III camera.

RESULTS

Study of $A\beta_{1–42}$ at early stages of aggregation

An aliquot of solubilized $A\beta_{1–42}$ was dissolved in PB to a final concentration of 10 μM and immediately visualized in liquid medium on mica substrate by tapping mode AFM. At this initial stage of incubation (t_0), the sample contained homogeneously distributed globular aggregates (Fig. 1*A*), in agreement with existing data (6–8, 10, 24, 25). The height of the aggregates was ~5 nm, and their deconvoluted diameter was 4.4 ± 0.4 nm (number of measurements made, n=425). Before application of the deconvolution Eq. [1] defined in Materials and Methods, the apparent diameter of the aggregates was found to be 18.8 ± 5.7 nm. When imaged at t_0 on a hydrophobic substrate such as highly ordered pyrolytic graphite (HOPG), $A\beta_{1–42}$ forms a layer 1 to 2 nm in

height (Fig. 1*B*), with globular and larger aggregates deposited on top of it. This layer is not observed on mica, suggesting that its formation is induced by the interaction of $A\beta_{1-42}$ with hydrophobic HOPG. Another aliquot of the t_0 sample was analyzed by Western blot after electrophoresis in SDS-containing polyacrylamide gels (Fig. 1*C*). The band with highest electrophoretic mobility corresponded to a molecular mass roughly coincident with that of the $A\beta_{1-42}$ monomer (4.5 kDa). Three minor bands of lower electrophoretic mobility were detected, with apparent approximate masses of 7, 16, and 20 kDa, that most likely correspond to the dimer, trimer, and tetramer species, respectively, of $A\beta_{1-42}$ that have resisted dissociation by SDS (10, 19, 22). The most abundant species detected at t_0 in immunoblots was a wide band with an apparent mobility of ~60 kDa, that probably corresponds to larger heterogeneous SDS-resistant oligomers.

$A\beta_{1-42}$ protofibrils

The next step in the process of Aβ aggregation is the appearance of the first fibrillar species, henceforth called *protofibrils,* in agreement with other authors (12, 16, 17, 19, 23). $A\beta_{1-42}$ samples incubated for 24 h and deposited on freshly cleaved mica or HOPG immediately before AFM imaging in liquid revealed the presence of protofibrils (Fig. 2*A*), ~1.5 nm in height and 9.3 ± 2.1 nm wide (n=684) before deconvolution. If this apparent width corresponded to a cylindrical structure, the deconvolution Eq. [1] could be applied, giving an estimated real diameter of 1.1 nm. Later, in the manuscript, however, we present evidence for a protofibril real width around 5.5 nm (see Fig. 3*G*), suggesting that the shape of protofibrils on HOPG is closer to a ribbon (~5.5 nm wide and ~1.5 nm high) than to a cylinder. Throughout our incubations up to 96 h protofibrils had an average length of 64.4 ± 18.5 nm (n=257), seldom exceeding 100 nm, and were visualized in much greater numbers when deposited on HOPG (Fig. 2*B*). This last observation suggests that they have a hydrophobic surface and therefore settle down more efficiently on hydrophobic graphite rather than on hydrophilic mica.

Protofibrils were observed to align in parallel forming bundles of up to 6 units that on HOPG were generally oriented following a three-fold symmetry (Fig. 2*B*). This pattern has been suggested to be an effect of the crystal structure of graphite that would act as a template to orient certain molecules along three directions at 120° to one another (21, 24). Such template-directed assembly induced by the hexagonal graphite lattice has also been described for the β-sheet-containing, de novo designed protein 17-6 (33), thus reinforcing the hypothesis that the observed patterning is indeed the result of the interaction of HOPG with any protein enriched in β-sheets. Protofibril bundles can assemble end-to-end to form longer structures (Fig. 2*C*). As an attempt to overcome the poor binding of protofibrils to mica, $A\beta_{1-42}$ in the samples from Fig. 2*A* and 2*C* was incubated in 10 mM acetate, pH 5.0. By doing so, our objective was to have a higher concentration of protofibrils in the solution, since Aβ fibrillogenesis in the absence of template is favored at a pH close to 5 (34).

$A\beta_{1-42}$ fibrils

It is generally accepted that Aβ protofibrils associate to form fibrils (11, 18–20, 23), which represent the highest structurally defined units described until now for Aβ fibrillogenesis. Abundant fibrils with a mean width of 11.4 ± 0.8 nm (n=430) (30.1±7.7 nm before deconvolution) are observed in $A\beta_{1-42}$ preparations after 2 days of incubation (Fig. 3*A*). The

length of fibrils ranges from a few hundreds of nanometers to some microns, exceeding sometimes 5 μm. Although protofibril bundle formation might be the initial step for fibril assembly, it is likely that individual protofibrils can also be incorporated into existing fibrils, as suggested by the observation of contacts between protofibril ends and fibrils (Fig. 3*B*). We have identified two main types of $A\beta_{1-42}$ fibrils according to their contour: smooth and nodular. Nodular fibrils are the dominant type up to 3.5 days of incubation, being the length of nodular fibril stretches ~10 times that of smooth sections. The two fibrils shown in Fig. 3*C*, one smooth (right) and one nodular (left), were imaged in the same scan, thus ruling out possible tip artifacts. Both fibril types started to appear simultaneously with protofibrils, and they were observed to grow in number and length with time. Currently, we cannot determine whether smooth and nodular fibrils correspond to sequential stages in a single linear aggregation process or if they represent different structures formed through distinct coexisting parallel pathways.

Nodular fibrils (Fig. 3*C*, 3*D*) have regularly spaced constrictions every 93.5 ± 21.0 nm (n=180). Longitudinal sections of the nodular and smooth fibrils from Fig. 3*C* are shown in Fig. 3*E* and 3*F*, respectively. The nodular fibril exhibits a characteristic periodic profile in contrast with the longitudinal section of the smooth fibril, which shows no periodicity. Smooth fibrils have a height of ~5 nm, whereas the height of nodular fibrils varies between ~11 nm in the center of the nodules and ~5 nm at internodal points. A higher-resolution scanning of the nodular fibril from Fig. 3*C* reveals a grooved surface (Fig. 3*D*) that delineates six elongated structures within each nodule (Fig. 3*G*). On the basis of images of intermediate species such as that shown in Fig. 2*C*, we deduce that the elongated structures are protofibrils. The number of protofibrils in the nodules has been observed to be 4 to 6, and the separation between the grooves running parallel to the fibril axis is 5.5 ± 1.1 nm (n=424). As these structures are one right next to the other instead of being isolated, deconvolution is not required, and we consider this distance the real protofibril width because it is not affected by preconceptions about the shape of the imaged structures or the radius of the tip apex. Scanning tunneling microscopy images of $A\beta_{1-42}$ fibrils on HOPG taken in air have also revealed an internal structure composed of elongated protofibrils or protofilaments (21).

AFM imaging in liquid on HOPG has given us a better structure resolution and a higher number of fibrils adsorbed per surface unit, but nodular fibrils in liquid are also observed on mica (Fig. 3*H*). When observed in air on mica, some fibrils appear to be composed of an assembly of the globular aggregates that are the dominant species at early times when the image is taken on a mica substrate (Fig. 3*I*). However, although such images might reveal particular features that are not observed on HOPG, AFM visualizations in air are prone to structural artifacts induced by the drying step.

Besides nodular and smooth types we have identified other fibril forms like that in Fig. 3*J*, where the constrictions are less pronounced than in the nodular type, hinting that such structures could be a transient species in a possible pathway having smooth fibrils as the end form. Figure 3*K* shows a fibril where the nodules are slightly tilted, thus giving to the structure a twisted or helical appearance. Left-handed helical structures formed by two or more strands are frequently observed in our in vitro preparations visualized by AFM and transmission electron microscopy (TEM) (Fig. 4). Each helix strand observed by TEM was 3.7 ± 0.7 nm across (n=714), and the whole structure ranged from this narrowest width to 7.6 ± 1.2 nm (n=774) at the widest point of the helix. The period of half an helix turn (i.e., the distance between two consecutive narrow

spots of the helix) differed between individual fibrils, varying from 39.0 to 149.4 nm, with a mean value of 92.5 ± 20.3 nm (n=219). Each helix strand has a width close to that of protofibrils, but it can reach a length of several microns, and we will thus refer to each strand as *protofilament*. Occasionally, AFM images could be obtained with an involuntarily split tip that enabled us to improve resolution by means of diminishing the tip apex radius. The tip was fractured in such a way that two different spikes were scanning the surface, one of them very sharp. Figures 4*A* and 4*B* are typical double tip images of protofilament helices where objects appear repeated. This helical structure has also been observed with undamaged tips (data not shown), although a lower resolution is obtained. Helices are often aligned side by side (Fig. 4*A*, *D–G*), suggesting that fibrils can grow in width trough the lateral association of protofilaments. Some TEM images show merging helices that straighten up into structures without an evident periodic twist (Fig. 4*E*).

Figure 5*A* shows an AFM image of partially assembled/disassembled fibrils, where the fibril nodules are hinted by the presence of apparently softer material that can be significantly pushed aside when applying greater forces with the AFM tip by increasing the working amplitude (Fig. 5*B*). This manipulation of fibrils revealed the existence of an underlying protofilament helix with a period that coincides precisely with the length of nodules in the fibril being imaged. Eventually, AFM and TEM images show fibrils that have been fractured in sections (Fig. 5*C–E*) with a mean fragment length of 107.3 ± 29.0 nm (n=172), close to the measured periodicities of fibril nodules (93.5±21.0 nm), and of the helical repeat of intertwined protofilaments (92.5±20.3 nm) (Fig. 5*F*). In these segmented fibrils, the two clearly discerned protofilaments run parallel and do not present any twist (Fig. 5*C*), and the protofilament sections strongly resemble protofibrils ~100 nm long (compare with inset in Fig. 2*B*). Although such fragmentation events might be due to the physical stress experienced by fibrils as a result of manipulation, they show evidence of the existence of a structural weakness related to the joining points between the constituent ~100-nm protofibril subunits.

DISCUSSION

It is likely that the most abundant features revealed at the onset of $A\beta_{1–42}$ fibrillogenesis by AFM on mica (globular aggregates) and by Western blots (~60-kDa band) correspond to the same molecular entity. This is in agreement with existing data indicating that, in a hydrophilic environment, $A\beta_{1–42}$ has a strong tendency to self-associate, forming the highly stable oligomeric structures termed ADDLs (7–9, 20). The globular aggregates visualized on mica have been suggested to be the result of the formation of pseudomicellar structures of an amphipathic molecule such as Aβ on a hydrophilic substrate (24). As pointed out by Chromy et al. (7), globules of 5 nm diameter are consistent with structures containing 6–9 $A\beta_{1-42}$ units, whereas the largest 8-nm globules might correspond to a 24mer that is often accepted as the upper limit for ADDL size (9). The $A\beta_{1–42}$ oligomers detected in immunoblots around 60 kDa would correspond to about the mass of 13 peptide molecules if they were linked in a string. However, in SDS-resistant aggregates the oligomers might adopt a nonlinear conformation that will confer anomalous molecular mass/mobility ratios (35). According to detailed electrophoretic studies (7, 20), $A\beta_{1–42}$ forms two distinct ADDL populations whose roles in AD pathogenesis are still not well understood: small oligomers consisting of monomers to pentamers/hexamers (4–25 kDa), and large globular amyloids containing up to 24mers (~60 kDa and above). Our wide ~60 kDa band likely represents an heterogeneous population of these large ADDLs. Stable $A\beta_{1–42}$

oligomers in aqueous solution could be the molecular entity responsible for the elevated neurotoxicity associated to soluble globular aggregates (7, 8). Small ADDLs include associations of four to six $A\beta_{1\text{-}42}$ units that have been described to form in the membrane of neurons the calcium-permeable channels suspected to be one of the causes of cell death associated to Aβ (22). As an alternative mechanism recently described, ADDLs between 10 and 100 kDa have been shown to bind to certain synapses (5). The ensuing functional disruption may provide a molecular basis for synapse failure in memory loss.

The protofibril dimensions deduced from AFM images (~1.5 nm high and ~5.5 nm wide) are in agreement with previous studies of $A\beta_{1\text{-}42}$ fibrillogenesis (21, 24). Several structural models have been proposed for amyloid protofibrils based on a variety of experimental techniques and theoretical models (13, 24, 36–44). Despite their divergence, all models agree that Aβ protofibrils are formed by a stacking of β-strands perpendicular to the axis of the protofibril, with a spacing of ~5 Å between consecutive hydrogen bond-linked β-strands. Most models derived from spectroscopy and diffraction data (37–39, 42, 43) propose structures where Aβ is forming a hairpin, with the resulting protofibril having a width of around 6 nm, in agreement with our empirical measurements for $A\beta_{1\text{–}42}$. This is consistent with a model where protofibrils on HOPG are single β-sheets formed by β-strands of $A\beta_{1\text{-}42}$ in the hairpin conformation (Fig. 6*A*), as suggested in the models proposed by Li et al. (43) and by Petkova et al. (39). In the first case (Fig. 6*A*, left) both β-strands of the hairpin are lying on the graphite surface, whereas in the second case (Fig. 6*A*, right) only one of the two β-strands is in contact with the surface. Although in Fig. 6*A* the peptide hairpins are represented in antiparallel orientation our data do not provide information about this issue. AFM images obtained on HOPG indicate that in aqueous medium $A\beta_{1\text{-}42}$ protofibrils have a high affinity for hydrophobic surfaces. Interactions between Aβ solubilized in an aqueous solution and hydrophobic surfaces (i.e., a hydrophilic/hydrophobic interface) may be important under physiological conditions within the amphipathic environments of biological membranes (15, 45) and of lipoprotein particles, since a significant amount of soluble Aβ is localized to lipoproteins in both plasma and the cerebrospinal fluid (46, 47). The use of hydrophilic (mica) and hydrophobic (HOPG) surfaces for AFM imaging has allowed us to identify two possible ways by which Aβ fibrils can grow: by direct addition of monomers or small globular oligomers and by addition of protofibrils that, in turn, were previously assembled from Aβ monomers and/or oligomers. As previously suggested by Goldsbury et al. (18), both processes could coexist in vivo, thus conciliating alternative models of fibril growth (16, 17, 19, 20, 37).

The mean length of isolated protofibrils is ~64 nm, and they do seldom grow longer than 100 nm. This observation can be explained by a selective channeling of longer protofibrils approaching 100 nm toward their incorporation into bundles (Fig. 6*B*, step *iii*), as suggested by the left-skewed histogram in Fig. 5*F* corresponding to the distribution of protofibril lengths. We have identified three other species in the $A\beta_{1\text{–}42}$ fibrillogenetic pathway that share a ~100-nm structural unit, namely, fibril nodules, helical protofilaments, and fibril fragments. Taken together, our data are consistent with the existence of a ~100-nm long protofibril species with a role as short-lived assembly intermediate whose elongation rate is slower than its rate of association to form fibrils (16). The presence of a variety of fibrillar entities (smooth, nodular, tilted, and intermediate forms) reinforces the view that $A\beta_{1\text{–}42}$ fibrillogenesis is a complex process that can unfold through multiple steps and several alternative pathways (16, 17). Lateral association of protofibrils is likely driven by the thermodynamically unfavorable exposure of the

constituent hydrophobic β-sheets to the aqueous environment. We have observed that 4 to 6 protofibrils associate side by side into bundles where the nonpolar C-terminal sequences could be shielded by the mostly hydrophilic N-terminal domains of Aβ (44). The bundles stack end-to-end (Fig. 6*B*, step *iv*) and appear to be capable of undergoing internal rearrangements leading to the generation of nodular fibrils (Fig. 6*B*, step *v*) and of a helical structure (Fig. 6*B*, step *vi*) that might play an important role in fibrillogenesis. We have observed a variety of helical periods that probably correspond to different points of coiling in the dynamic process leading from protofibrils to protofilaments and fibrils. Conformational changes experienced by protofibrils turning into protofilaments could be responsible for the different dimensions of isolated protofibrils (short ribbonlike structures ~5.5 nm wide and ~1.5 nm high) and of protofilaments (long cylinders ~4 nm in diameter). A wide range of coiled and non-coiled protofilaments has been also observed by other authors in TEM and AFM images of $A\beta_{1\text{-}40}$ and $A\beta_{1\text{–}42}$ preparations (16–18).

Nodular fibrils might evolve further by joining their segments to yield smooth fibrils (Fig. 6*B*, step *vii*), although conclusive evidence for this sequence can only be provided by time-lapse AFM approaches that are currently under way. Dynamic AFM studies will also help to clarify whether the steps proposed in the model depicted in Fig. 6*B* can also be reversible, as suggested by in vitro studies of the fibrillization of Aβ (48) and of other amyloid fibril-forming proteins like α-synuclein and transthyretin (49). A structural organization similar to that observed for $A\beta_{1\text{-}42}$ in protofilament helices and fibril nodules has been described for other types of amyloid fibrils produced in vitro from very different polypeptide sequences such as lysozyme and the 90-residue Src homology (SH3) domain of bovine phosphatidylinositol-3′-kinase (50). Although Aβ, lysozyme, SH3, and a number of other amyloidogenic proteins and peptides (36) are not sequence-related, they form twisted protofilaments and nodular fibrils remarkably similar in periodicity, dimensions, and number of constituent subunits. This is in agreement with the current view that, despite the different nature of precursor proteins and peptides, amyloid fibrils represent a structural superfamily and share a common protofilament structure (36, 51, 52).

ACKNOWLEDGMENTS

This work was supported by grant BIO2002-00128 from the Ministerio de Ciencia y Tecnología (MCyT), Spain, that included FEDER funds. X.F.-B. holds a Ramón y Cajal tenure track position from the MCyT. We thank the Scientific and Technical Services of the University of Barcelona for technical assistance. We are indebted to Montserrat Cruz and to Dolors Grillo-Bosch for helpful discussions.

REFERENCES

1. Yankner, B. A. (1996) Mechanisms of neuronal degeneration in Alzheimer's disease. *Neuron* **16,** 921–932

2. Pollard, H. B., Rojas, E., and Arispe, N. (1993) A new hypothesis for the mechanism of amyloid toxicity, based on the calcium channel activity of amyloid β protein (AβP) in phospholipid bilayer membranes. *Ann. N. Y. Acad. Sci.* **695,** 165–168

3. Bhatia, R., Lin, H., and Lal, R. (2000) Fresh and globular amyloid β protein (1-42) induces rapid cellular degeneration: evidence for AbetaP channel-mediated cellular toxicity. *FASEB J.* **14,** 1233–1243

4. Zhu, Y. J., Lin, H., and Lal, R. (2000) Fresh and nonfibrillar amyloid β protein(1-40) induces rapid cellular degeneration in aged human fibroblasts: evidence for AbetaP-channel-mediated cellular toxicity. *FASEB J.* **14,** 1244–1254

5. Lacor, P. N., Buniel, M. C., Chang, L., Fernandez, S. J., Gong, Y., Viola, K. L., Lambert, M. P., Velasco, P. T., Bigio, E. H., Finch, C. E., et al. (2004) Synaptic targeting by Alzheimer's-related amyloid β oligomers. *J. Neurosci.* **24,** 10,191–10,200

6. Hu, J., Akama, K. T., Krafft, G. A., Chromy, B. A., and Van Eldik, L. J. (1998) Amyloid-β peptide activates cultured astrocytes: morphological alterations, cytokine induction and nitric oxide release. *Brain Res.* **785,** 195–206

7. Chromy, B. A., Nowak, R. J., Lambert, M. P., Viola, K. L., Chang, L., Velasco, P. T., Jones, B. W., Fernandez, S. J., Lacor, P. N., Horowitz, P., et al. (2003) Self-assembly of Abeta(1-42) into globular neurotoxins. *Biochemistry* **42,** 12,749–12,760

8. Stine, W. B., Jr., Dahlgren, K. N., Krafft, G. A., and LaDu, M. J. (2003) In vitro characterization of conditions for amyloid-β peptide oligomerization and fibrillogenesis. *J. Biol. Chem.* **278,** 11,612–11,622

9. Klein, W. L. (2002) Abeta toxicity in Alzheimer's disease: globular oligomers (ADDLs) as new vaccine and drug targets. *Neurochem. Int.* **41,** 345–352

10. Dahlgren, K. N., Manelli, A. M., Stine, W. B., Jr., Baker, L. K., Krafft, G. A., and LaDu, M. J. (2002) Oligomeric and fibrillar species of amyloid-β peptides differentially affect neuronal viability. *J. Biol. Chem.* **277,** 32,046–32,053

11. Serpell, L. C. (2000) Alzheimer's amyloid fibrils: structure and assembly. *Biochim. Biophys. Acta* **1502,** 16–30

12. Walsh, D. M., Hartley, D. M., Kusumoto, Y., Fezoui, Y., Condron, M. M., Lomakin, A., Benedek, G. B., Selkoe, D. J., and Teplow, D. B. (1999) Amyloid β-protein fibrillogenesis. Structure and biological activity of protofibrillar intermediates. *J. Biol. Chem.* **274,** 25,945–25,952

13. Roher, A. E., Baudry, J., Chaney, M. O., Kuo, Y. M., Stine, W. B., and Emmerling, M. R. (2000) Oligomerization and fibril asssembly of the amyloid-β protein. *Biochim. Biophys. Acta* **1502,** 31–43

14. Antzutkin, O. N. (2004) Amyloidosis of Alzheimer's Abeta peptides: solid-state nuclear magnetic resonance, electron paramagnetic resonance, transmission electron microscopy, scanning transmission electron microscopy and atomic force microscopy studies. *Magn. Reson. Chem.* **42,** 231–246

15. Yip, C. M., Darabie, A. A., and McLaurin, J. (2002) Abeta42-peptide assembly on lipid bilayers. *J. Mol. Biol.* **318,** 97–107

16. Harper, J. D., Wong, S. S., Lieber, C. M., and Lansbury, P. T. (1997) Observation of metastable Abeta amyloid protofibrils by atomic force microscopy. *Chem. Biol.* **4,** 119–125

17. Harper, J. D., Lieber, C. M., and Lansbury, P. T., Jr. (1997) Atomic force microscopic imaging of seeded fibril formation and fibril branching by the Alzheimer's disease amyloid-β protein. *Chem. Biol.* **4,** 951–959

18. Goldsbury, C. S., Wirtz, S., Muller, S. A., Sunderji, S., Wicki, P., Aebi, U., and Frey, P. (2000) Studies on the in vitro assembly of Aβ 1-40: implications for the search for Aβ fibril formation inhibitors. *J. Struct. Biol.* **130,** 217–231

19. Walsh, D. M., Lomakin, A., Benedek, G. B., Condron, M. M., and Teplow, D. B. (1997) Amyloid β-protein fibrillogenesis. Detection of a protofibrillar intermediate. *J. Biol. Chem.* **272,** 22,364–22,372

20. Bitan, G., Kirkitadze, M. D., Lomakin, A., Vollers, S. S., Benedek, G. B., and Teplow, D. B. (2003) Amyloid β-protein (Abeta) assembly: Abeta 40 and Abeta 42 oligomerize through distinct pathways. *Proc. Natl. Acad. Sci. USA* **100,** 330–335

21. Wang, Z., Zhou, C., Wang, C., Wan, L., Fang, X., and Bai, C. (2003) AFM and STM study of β-amyloid aggregation on graphite. *Ultramicroscopy* **97,** 73–79

22. Lin, H., Bhatia, R., and Lal, R. (2001) Amyloid β protein forms ion channels: implications for Alzheimer's disease pathophysiology. *FASEB J.* **15,** 2433–2444

23. Harper, J. D., Wong, S. S., Lieber, C. M., and Lansbury, P. T., Jr. (1999) Assembly of Aβ amyloid protofibrils: an in vitro model for a possible early event in Alzheimer's disease. *Biochemistry* **38,** 8972–8980

24. Kowalewski, T., and Holtzman, D. M. (1999) In situ atomic force microscopy study of Alzheimer's β-amyloid peptide on different substrates: new insights into mechanism of β-sheet formation. *Proc. Natl. Acad. Sci. USA* **96,** 3688–3693

25. Parbhu, A., Lin, H., Thimm, J., and Lal, R. (2002) Imaging real-time aggregation of amyloid β protein (1-42) by atomic force microscopy. *Peptides* **23,** 1265–1270

26. Zagorski, M. G., Yang, J., Shao, H., Ma, K., Zeng, H., and Hong, A. (1999) Methodological and chemical factors affecting amyloid β peptide amyloidogenicity. *Methods Enzymol.* **309,** 189–204

27. Laemmli, U. K. (1970) Cleavage of structural proteins during the assembly of the head of bacteriophage T4. *Nature* **227,** 680–685

28. Schagger, H., and von Jagow, G. (1987) Tricine-sodium dodecyl sulfate-PAGE for the separation of proteins in the range from 1 to 100 kDa. *Anal. Biochem.* **166,** 368–379

29. Stine, W. B., Jr., Snyder, S. W., Ladror, U. S., Wade, W. S., Miller, M. F., Perun, T. J., Holzman, T. F., and Krafft, G. A. (1996) The nanometer-scale structure of amyloid-β visualized by atomic force microscopy. *J. Protein Chem.* **15,** 193–203

30. Keller, D. (1991) Reconstruction of Stm and Afm images distorted by finite-size tips. *Surf. Sci.* **253,** 353–364

31. Gomez, E., Valles, E., Gorostiza, P., Servat, J., and Sanz, F. (1995) Electrodeposition of zinc-cobalt alloys-Tapping mode AFM technique applied to study the initial stages of deposition. *J. Electrochem. Soc.* **142,** 4091–4096

32. Vesenka, J., Guthold, M., Tang, C. L., Keller, D., Delaine, E., and Bustamante, C. (1992) Substrate preparation for reliable imaging of DNA molecules with the scanning force microscope. *Ultramicroscopy* **42,** 1243–1249

33. Brown, C. L., Aksay, I. A., Saville, D. A., and Hecht, M. H. (2002) Template-directed assembly of a de novo designed protein. *J. Am. Chem. Soc.* **124,** 6846–6848

34. Esler, W. P., Stimson, E. R., Ghilardi, J. R., Vinters, H. V., Lee, J. P., Mantyh, P. W., and Maggio, J. E. (1996) In vitro growth of Alzheimer's disease β-amyloid plaques displays first-order kinetics. *Biochemistry* **35,** 749–757

35. Kawooya, J. K., Emmons, T. L., Gonzalez-DeWhitt, P. A., Camp, M. C., and D'Andrea, S. C. (2003) Electrophoretic mobility of Alzheimer's amyloid-β peptides in urea-sodium dodecyl sulfate-PAGE. *Anal. Biochem.* **323,** 103–113

36. Serpell, L. C., Sunde, M., Benson, M. D., Tennent, G. A., Pepys, M. B., and Fraser, P. E. (2000) The protofilament substructure of amyloid fibrils. *J. Mol. Biol.* **300,** 1033–1039

37. Serpell, L. C., Blake, C. C., and Fraser, P. E. (2000) Molecular structure of a fibrillar Alzheimer's Aβ fragment. *Biochemistry* **39,** 13,269–13,275

38. Guo, J. T., Wetzel, R., and Xu, Y. (2004) Molecular modeling of the core of Abeta amyloid fibrils. *Proteins* **57,** 357–364

39. Petkova, A. T., Ishii, Y., Balbach, J. J., Antzutkin, O. N., Leapman, R. D., Delaglio, F., and Tycko, R. (2002) A structural model for Alzheimer's β-amyloid fibrils based on experimental constraints from solid state NMR. *Proc. Natl. Acad. Sci. USA* **99,** 16,742–16,747

40. Malinchik, S. B., Inouye, H., Szumowski, K. E., and Kirschner, D. A. (1998) Structural analysis of Alzheimer's β(1-40) amyloid: protofilament assembly of tubular fibrils. *Biophys. J.* **74,** 537–545

41. Benzinger, T. L., Gregory, D. M., Burkoth, T. S., Miller-Auer, H., Lynn, D. G., Botto, R. E., and Meredith, S. C. (2000) Two-dimensional structure of β-amyloid(10-35) fibrils. *Biochemistry* **39,** 3491–3499

42. Antzutkin, O. N., Leapman, R. D., Balbach, J. J., and Tycko, R. (2002) Supramolecular structural constraints on Alzheimer's β-amyloid fibrils from electron microscopy and solid-state nuclear magnetic resonance. *Biochemistry* **41,** 15,436–15,450

43. Li, L., Darden, T. A., Bartolotti, L., Kominos, D., and Pedersen, L. G. (1999) An atomic model for the pleated β-sheet structure of Abeta amyloid protofilaments. *Biophys. J.* **76,** 2871–2878

44. Chaney, M. O., Webster, S. D., Kuo, Y. M., and Roher, A. E. (1998) Molecular modeling of the Abeta1-42 peptide from Alzheimer's disease. *Protein Eng.* **11,** 761–767

45. Kawahara, M., and Kuroda, Y. (2000) Molecular mechanism of neurodegeneration induced by Alzheimer's β-amyloid protein: channel formation and disruption of calcium homeostasis. *Brain Res. Bull.* **53,** 389–397

46. Biere, A. L., Ostaszewski, B., Stimson, E. R., Hyman, B. T., Maggio, J. E., and Selkoe, D. J. (1996) Amyloid β-peptide is transported on lipoproteins and albumin in human plasma. *J. Biol. Chem.* **271,** 32,916–32,922

47. Koudinov, A. R., Koudinova, N. V., Kumar, A., Beavis, R. C., and Ghiso, J. (1996) Biochemical characterization of Alzheimer's soluble amyloid β protein in human cerebrospinal fluid: association with high density lipoproteins. *Biochem. Biophys. Res. Commun.* **223,** 592–597

48. Maggio, J. E., Stimson, E. R., Ghilardi, J. R., Allen, C. J., Dahl, C. E., Whitcomb, D. C., Vigna, S. R., Vinters, H. V., Labenski, M. E., and Mantyh, P. W. (1992) Reversible in vitro growth of Alzheimer disease β-amyloid plaques by deposition of labeled amyloid peptide. *Proc. Natl. Acad. Sci. USA* **89,** 5462–5466

49. Foguel, D., Suarez, M. C., Ferrao-Gonzales, A. D., Porto, T. C., Palmieri, L., Einsiedler, C. M., Andrade, L. R., Lashuel, H. A., Lansbury, P. T., Kelly, J. W., et al. (2003) Dissociation of amyloid fibrils of α-synuclein and transthyretin by pressure reveals their reversible nature and the formation of water-excluded cavities. *Proc. Natl. Acad. Sci. USA* **100,** 9831–9836

50. Chamberlain, A. K., MacPhee, C. E., Zurdo, J., Morozova-Roche, L. A., Hill, H. A., Dobson, C. M., and Davis, J. J. (2000) Ultrastructural organization of amyloid fibrils by atomic force microscopy. *Biophys. J.* **79,** 3282–3293

51. Sunde, M., Serpell, L. C., Bartlam, M., Fraser, P. E., Pepys, M. B., and Blake, C. C. (1997) Common core structure of amyloid fibrils by synchrotron X-ray diffraction. *J. Mol. Biol.* **273,** 729–739

52. Khurana, R., Ionescu-Zanetti, C., Pope, M., Li, J., Nielson, L., Ramirez-Alvarado, M., Regan, L., Fink, A. L., and Carter, S. A. (2003) A general model for amyloid fibril assembly based on morphological studies using atomic force microscopy. *Biophys. J.* **85,** 1135–1144

Fig. 1

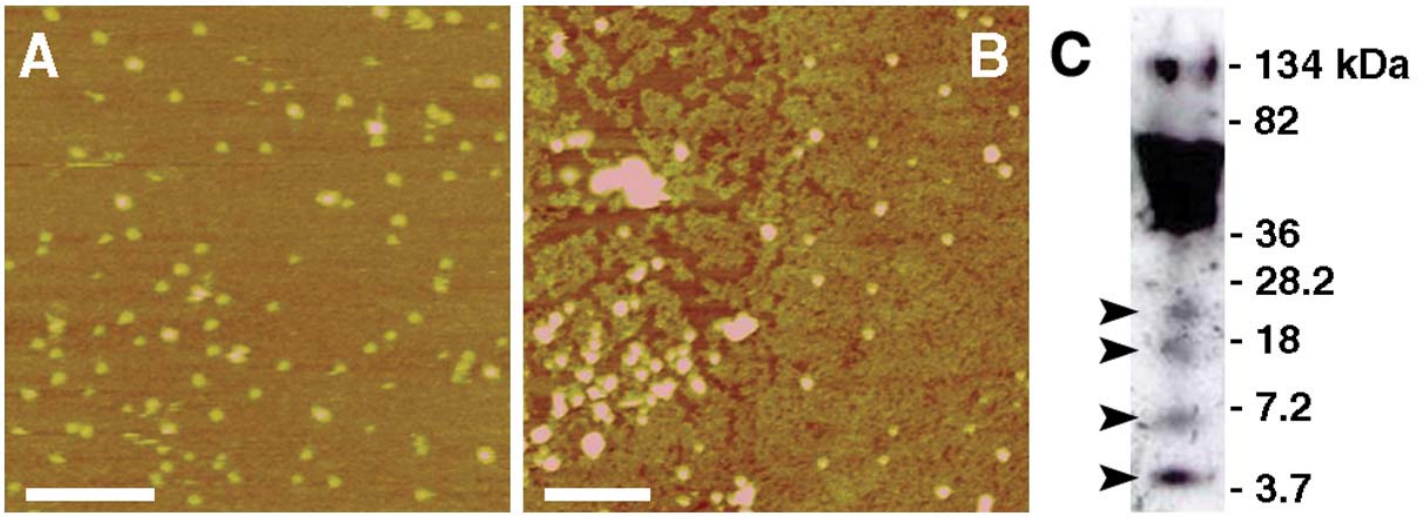

Figure 1. $A\beta_{1\text{-}42}$ at t_0. ***A, B***) Height atomic force microscopy (AFM) images of an $A\beta_{1\text{–}42}$ sample at t_0 visualized on mica (***A***) and on HOPG (***B***). ***C***) Immunoblot analysis of the same sample. Arrowheads indicate the positions of bands assigned (from bottom to top) to $A\beta_{1\text{-}42}$ monomer, dimer, trimer, and tetramer. Bar: 250 nm. Z scale: 20 nm (***A***) and 10 nm (***B***).

Fig. 2

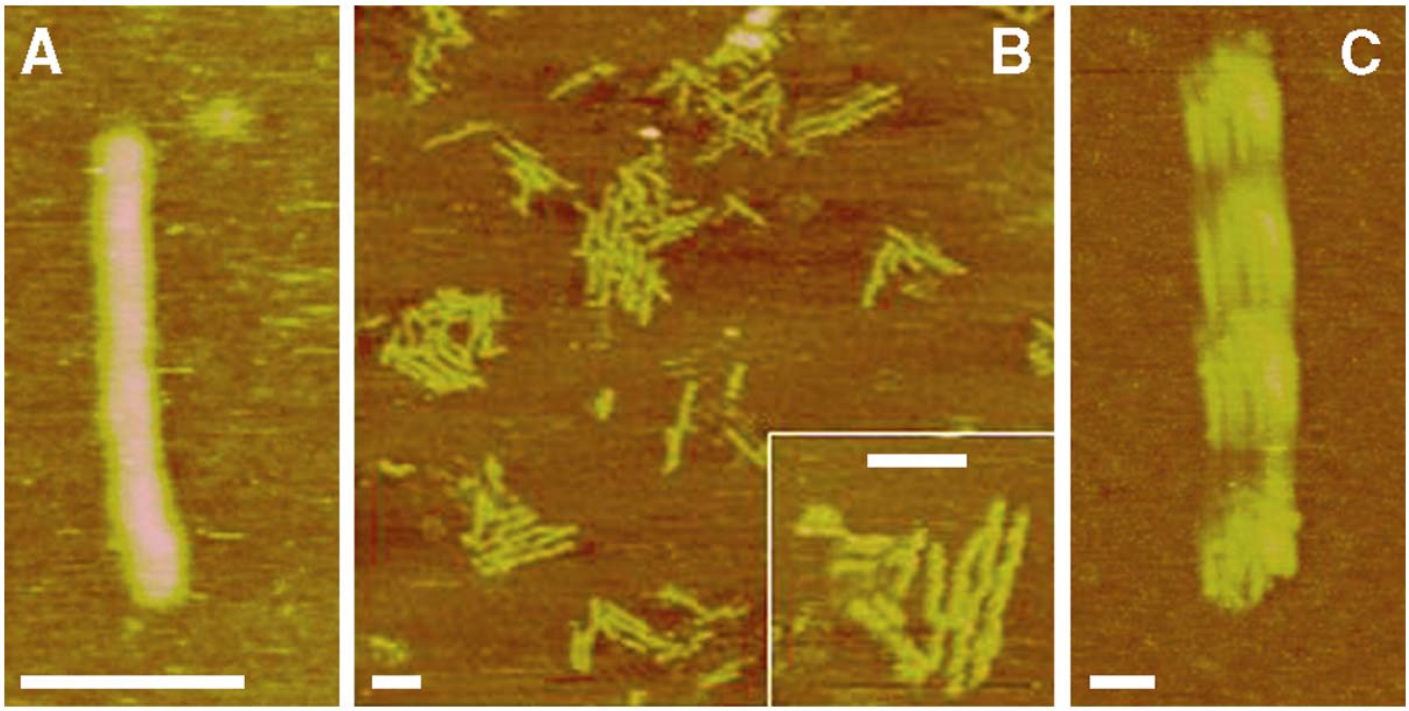

Figure 2. AFM images of $A\beta_{1-42}$ protofibrils. ***A*)** Single protofibril and globular structure on mica after an incubation time (t_i) of 20 h. ***B*)** Protofibril bundles on HOPG (t_i=2 days). ***C*)** End-to-end assembly of four protofibril bundles on mica (t_i=2 days). All images correspond to height AFM signal. The samples imaged on mica were incubated in 10 mM acetate buffer, pH 5.0. Bar: 50 nm. Z scale: 6 nm (***A***, ***B***), 5 nm (***B***, ***inset***), and 30 nm (***C***).

Fig. 3

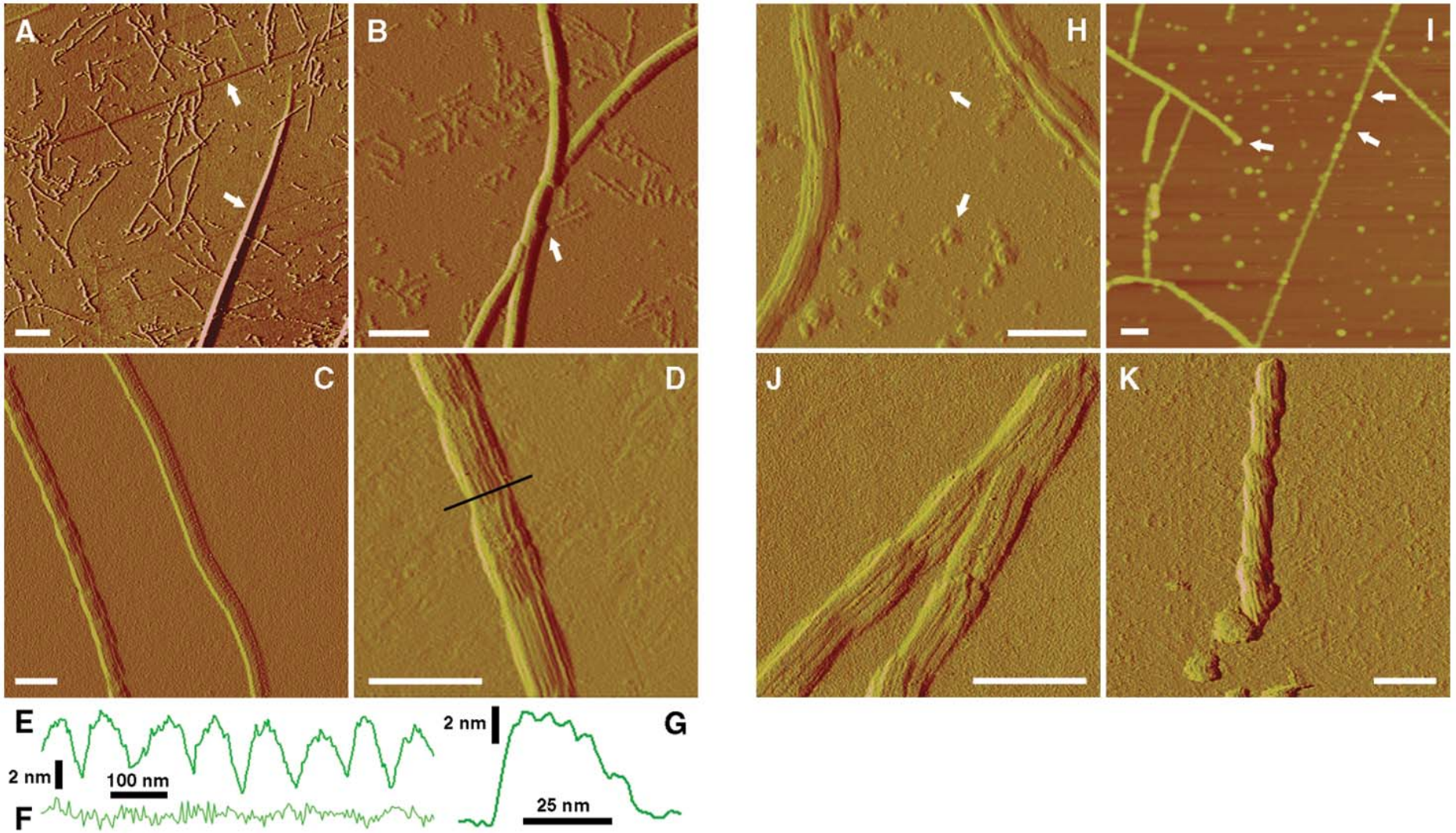

Figure 3. AFM images of $A\beta_{1-42}$ fibrils. ***A*)** Low-magnification image of fibrils. Arrows point steps in the graphite surface. ***B*)** Fibrils and protofibrils coexisting. The arrow shows contacts between a fibril and protofibril ends. ***C*)** Nodular and smooth fibrils. ***D*)** Nodular fibril from (***C***) scanned at higher resolution. The black line indicates the section corresponding to the topographic profile in (***G***). ***E, F***) Longitudinal topographic profiles of the nodular fibril (***E***) and smooth fibril (***F***) from (***C***). ***G*)** Transversal topographic profile of the nodular fibril from (***D***). ***H*)** Nodular fibrils visualized on mica in liquid. ***I*)** Fibrils visualized on mica in air. Arrows in (***H***) and (***I***) indicate typical globular structures visualized on mica. ***J*)** Intermediate form between nodular and smooth fibrils. ***K*)** Fibril with tilted nodules. All AFM images are presented as unprocessed amplitude signal, except image ***I*** (height signal) and were taken after 2 to 3.5 days of incubation. Images ***H*** and ***I*** were taken on mica and all others on HOPG. Bar: 1 μm for (***A***), 100 nm for all others. Z scale for (***I***): 20 nm.

Fig. 4

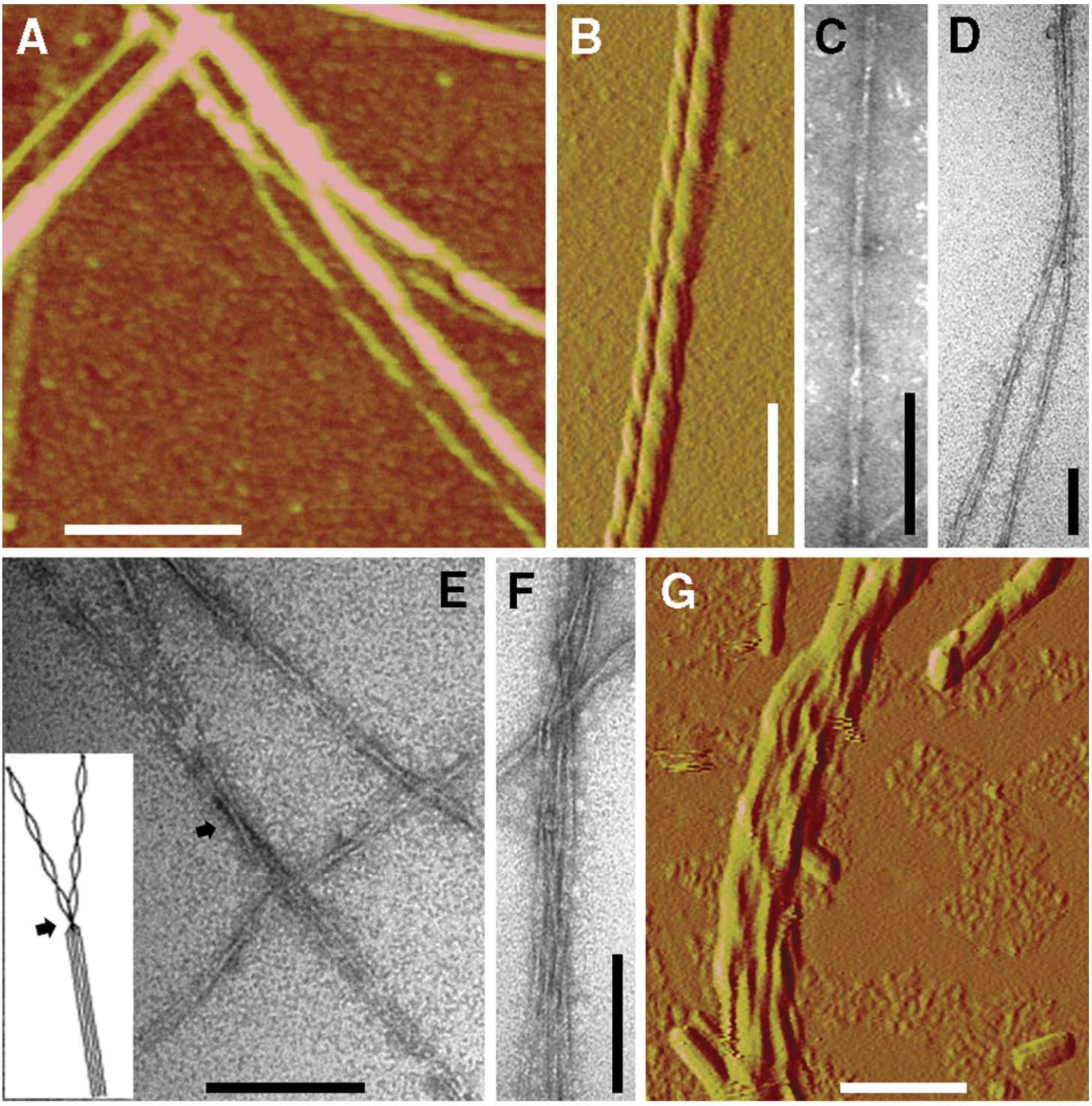

Figure 4. Helical structures formed by $A\beta_{1-42}$. Height (***A***) and amplitude (***B***) AFM images of helical structures obtained with a split tip. ***C-F***) transmission electron microscopy (TEM) images of (***C***) two intertwined protofilaments forming a helical structure, (***D, E***) two helical structures forming a four-protofilament species, and (***F***) an association of several helical structures; the arrows in (***E***) indicate in both model and TEM image the point where two pairs of intertwined protofilaments merge into a four-stranded, noncoiled fibril. ***G***) Amplitude AFM image of a group of merged fibrils having a helical structure. All AFM images were taken on HOPG. All samples were incubated for 2 days. Bar: 100 nm. Z scale for image (***A***): 12 nm.

Fig. 5

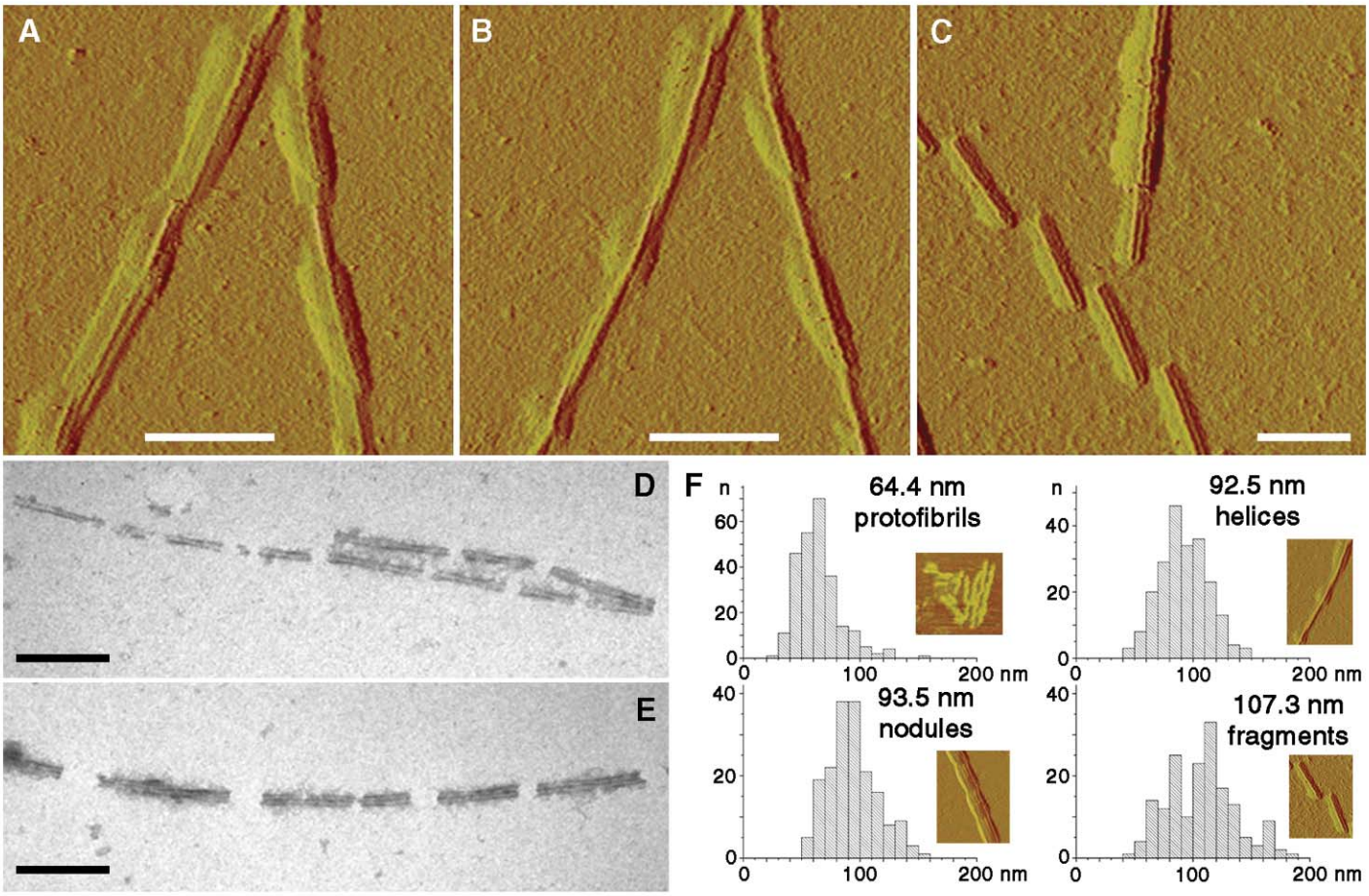

Figure 5. AFM manipulation of $A\beta_{1-42}$ fibrils and visualization of segmented fibrils. ***A, B***) Amplitude AFM images taken on HOPG of the same fibrils scanned with (***A***) low and (***B***) high amplitude, in order to increase force between tip and sample in the latter case. ***C***) Amplitude AFM image of a segmented fibril. ***D, E***) TEM images of segmented fibrils. All samples were incubated for 2 days. ***F***) Histogram representations of the lengths of a statistically significant number (*n*) of isolated protofibrils (from AFM data), fibril nodules (AFM), helical periodicities (TEM), and fibril fragments (AFM and TEM). Mean values of the respective distributions are indicated beside each histogram (standard deviations and number of measurements done are provided in the manuscript text). Bar: 100 nm.

Fig. 6

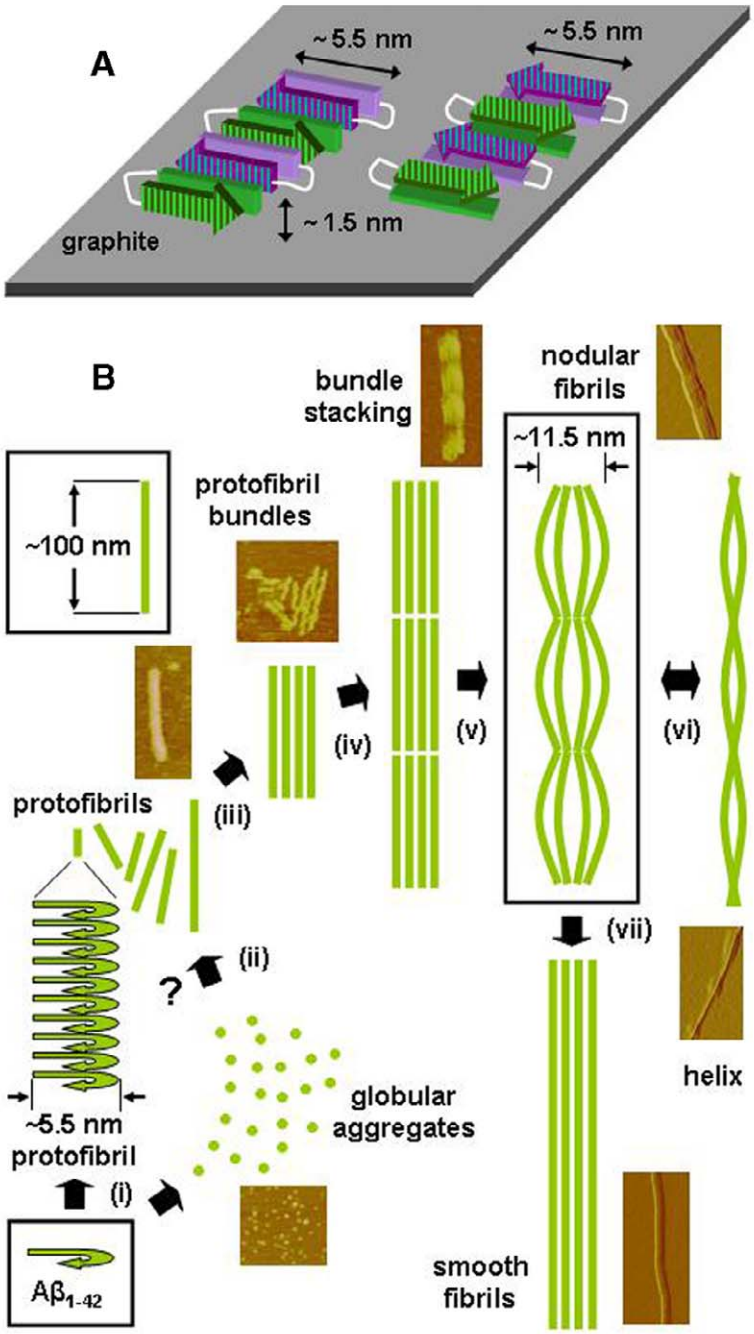

Figure 6. Proposed model for $A\beta_{1-42}$ fibrillogenesis in vitro. ***A*)** Cartoon illustrating two possible models for the formation of an $A\beta_{1-42}$ protofibril on HOPG. The height of the protofibril (~1.5 nm) is provided by the thickness of the peptide adopting a hairpin (for each model, 4 peptide molecules are represented), whereas the width of the protofibril (~5.5 nm) corresponds to the length of the hairpin. On the left scheme, both strands of the hairpin are in contact with the graphite, whereas on the right scheme, only one strand of the hairpin is facing the surface. ***B*)** Schematic model proposal of the different stages in the amyloid fibril formation process: ***i*)** monomeric $A\beta_{1-42}$ associates to form protofibrils and globular oligomers; the data presented here do not provide evidence for the incorporation of oligomers into growing protofibrils **(*ii*)**; protofibrils that reach ~100 nm can form bundles **(*iii*)**; through end-to-end stacking **(*iv*)**, bundles generate the nodular type fibrils **(*v*)**, which may be related to a helical structure formed by intertwined protofilaments **(*vi*)**; finally, nodular fibrils might evolve further to yield smooth fibrils (***vii***). To illustrate the model, we have included AFM images of the different structures.